Combinatorial growth of multinary nanostructured thin functional films

Hannah-Noa Barad, Mariana Alarcón-Correa, Gerardo Salinas, Eran Oren, Florian Peter, Alexander Kuhn, Peer Fischer

ELSEVIER

Combinatorial growth of multinary nanostructured thin functional films

Hannah-Noa Barad [1], Mariana Alarcón-Correa [1], Gerardo Salinas [3], Eran Oren [1], Florian Peter [1,2], Alexander Kuhn [3], Peer Fischer [1,2,*]

[1] Max Planck Institute for Intelligent Systems (MPI-IS), Heisenbergstr. 3, 70569 Stuttgart, Germany
[2] Institute of Physical Chemistry, University of Stuttgart, Pfaffenwaldring 55, 70569 Stuttgart, Germany
[3] Univ. Bordeaux, CNRS, Bordeaux INP, ISM, UMR 5255, 33607 Pessac, France

The rapid generation of material libraries with multidimensional gradients is important for the discovery of new functional materials. Here we report an integrated fabrication scheme, based on glancing angle physical vapor deposition, to form a thin-film materials library with controlled variations in nanoshape, multinary composition, and oxidation state on a single large area substrate. We demonstrate the versatility of the method by growing an octonary materials system, which we characterize with high-throughput methods, and reveal variations in several physico-chemical properties. Among others, we examine the materials library in the frame of the oxygen evolution reaction and show that nanostructuring leads to NiO clusters that are active towards such a reaction. Our scheme can be readily extended to include more starting elements, and can be transferred to other deposition methods, making this an adaptable and versatile platform for combinatorial materials science.

Keywords: Combinatorial materials science (CMS); Glancing angle deposition (GLAD); Compositional spread; Nanostructuring; Oxygen evolution reaction (OER)

Introduction

Material composition, micro- and nanostructure, as well as chemical state are important parameters that determine the functionality of many high-performance material systems. Increasing the number of constituting elements has been shown to influence properties such as luminescence [1], electrocatalysis [2,3], and, for instance, superconductivity [4], where multinary elemental systems exhibit higher critical temperatures. As many of the compositional spaces for binary and ternary systems have already been explored, it is expected that increasing the number of elements in a system will lead to interesting discoveries [5], which could include new active materials, or new systems containing materials with different activities. Variations in material composition on a single substrate have been studied using combinatorial materials science (CMS) as a method [6–8]. CMS is applied to thin-films, where a single substrate is coated with several material gradients in one experiment to form a materials library (ML) with variations of different deposition parameters, namely composition, thickness, and temperature. The synthesis is usually performed by physical vapor deposition (PVD) techniques, where it is easy to control the vapor flux by setting the power or by using shadow masks to induce gradient formation [9,10].

Although, composition is a highly studied parameter in CMS, other parameters, including morphology and chemical state, have not been investigated extensively. The chemical state is crucial for a number of material characteristics, including chemical reactivity, conductivity, and magnetism. Some CMS experiments have used X-ray photoelectron spectroscopy (XPS) to investigate

* Corresponding author.
E-mail address: Fischer, P. (fischer@is.mpg.de)

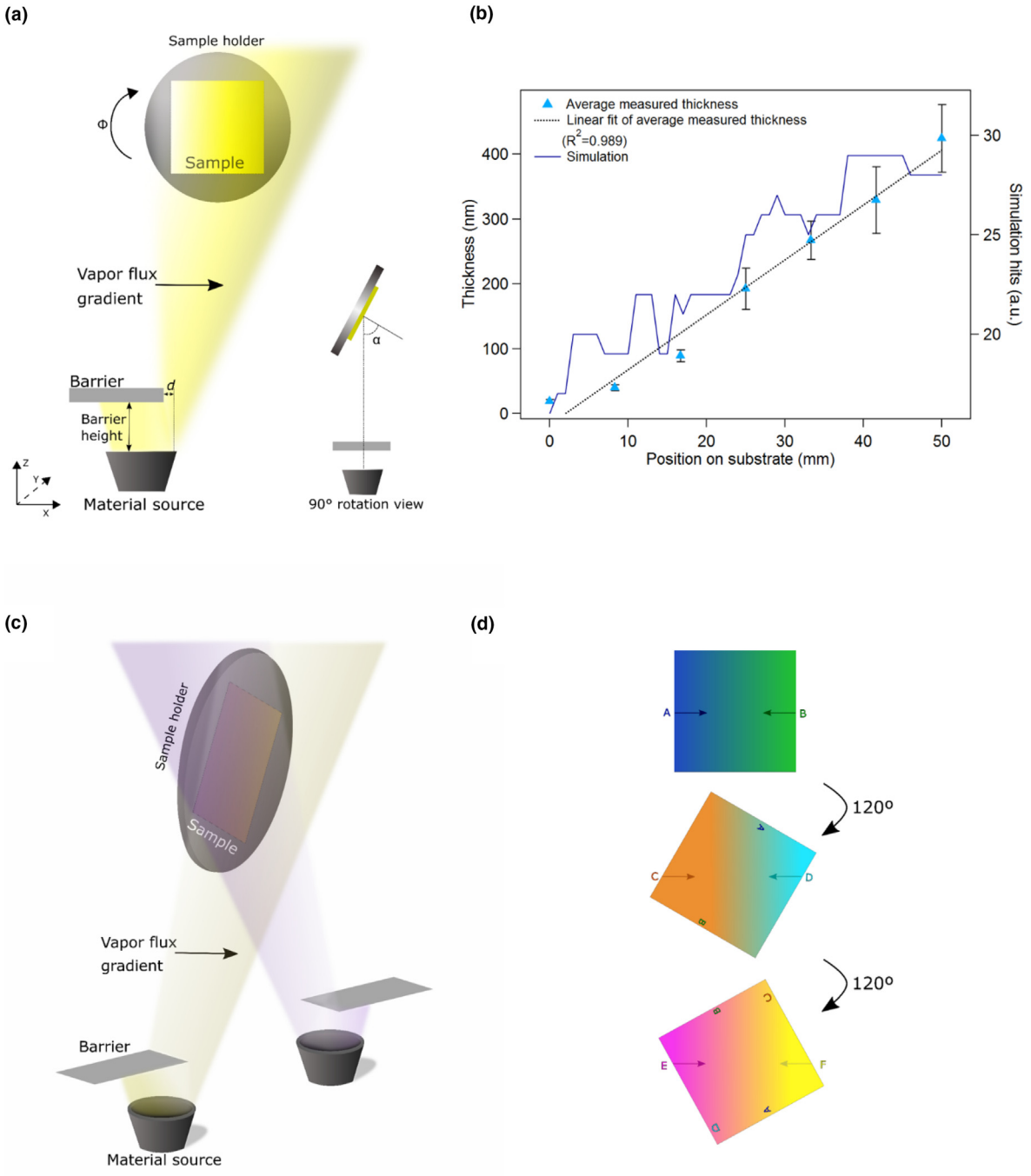

FIGURE 1

Illustration of CMS-GLAD system setup. (a) Positioning of the material source relative to the substrate center and placement of a barrier in the vapor flux path. On the *x*-axis the material source and substrate are placed off-axis, while on the *y*-axis their centers are aligned. This positioning, together with the barrier placement, forms a vapor flux gradient with a linear profile. The barrier height above the material source and the distance from the barrier edge to the exposed vapor flux edge, *d*, are marked. Along with the distance between the material source and substrate (*z*-axis), these positions influence the profile of the vapor gradient. Bottom right is a 90° view of the setup, where the α angle, important for the shadow growth formation of 3D-nanostructures, is marked. (b) Monte Carlo simulation of a linear gradient, and measurements of a linear thickness gradient deposited over a length of 50 mm. Error bars were calculated based on the standard deviation of the average thickness from all the thickness measurements taken at a given point. (c) Co-deposition configuration for a binary material system, with a second material source placed off-axis with respect to the substrate center (*x*-axis) with an additional barrier to form a linear vapor flux gradient. (d) Schematic of three sequential binary co-depositions with linear material gradients. After each deposition the substrate is rotated by 120° for the following binary co-deposition. The arrows point along the direction of a given material gradient from high (flat end) to low (arrowhead).

surfaces and interfaces during synthesis [11,12], or to understand chemical state environments after deposition [13,14]. As for the combinatorial microstructure of thin films, studies have shown the ability to construct structure zone diagrams [13] and to understand the effects of compositional changes on the microstructural properties of compact thin films [15–18]. How-

ever, to the best of our knowledge, there have been no CMS studies on thin films composed of varying nanostructures (*i.e.* not compact thin films and not films made of large microstructures, which have been examined before, discussed hereinafter).

Nanostructuring of materials affects attributes that relate to surface area and energetics, which are important for catalysts [19], batteries, photovoltaics [20], and thermoelectrics [21]. Similarly, the nanoshape plays a major role in the melting-point [22] and for tuning the optical extinction, specifically in metallic nanoparticles, where different shapes possess vastly different spectral characteristics [23]. Furthermore, complex nanostructures with multi-elemental active systems, each playing a different role in the overall device activity, are already showing promise for photocatalytic applications [24]. It is therefore necessary to increase the complexity of thin-film materials libraries such that they not only show variations in material or compound composition, thickness, and chemical state, but also show controlled gradients in nanostructuring.

Here, we establish a rapid integrated experimental approach to fabricate nanostructures on large areas with continuous changes in material composition, nanoshape, and chemical state, by combining CMS with glancing angle deposition (GLAD). Our approach is not confined to the commonly investigated binary or ternary material systems, but can be readily extended to include many more elements forming multinary MLs. The rationale behind the choice of materials for the ML is that they have all demonstrated activity (under different configurations) towards oxygen evolution reaction (OER), which is our model application for demonstrating our approach; as we wanted to examine the effects of compositional gradients as well as nanostructuring, which are both important in OER. We establish a growth scheme that rapidly and reproducibly generates multidimensional gradients, including in terms of nanostructure, which should facilitate the discovery of new materials with interesting potential applications. We also show that NiO nanoclusters, embedded in different nanostructures, are promising for the oxygen evolution reaction.

Thin-film growth is routinely performed with physical vapor deposition (PVD) techniques, which have been optimized to grow homogenous thin films that show little change across the substrate. For CMS it is necessary that compositional gradients are obtained, which requires an off-axis geometry, such that the vapor flux varies across the substrate during deposition. In order to also incorporate nanostructuring in the ML, GLAD may be used. GLAD is a physical vapor deposition method where the substrate in a sputtering or electron beam vacuum system is simultaneously rotated and tilted so that the incoming vapor flux is incident at grazing angles [25]. The angular shadow growth allows for the formation of 3D-shaped nanostructures [26,27], and is therefore promising for CMS. However, to date, only a few studies have used GLAD in combination with CMS. Two groups [28,29] have examined binary or ternary material compositions, while another one examined a ternary system, but not on a single large-area substrate [30]. One study discussed micro surface-structuring, as well as the composition of a binary system [31], and another evaluated thickness changes for plasmonic Au nanoparticle dimers [32]. In order to combine in a single experiment the synthesis of a multinary ML (beyond ternary) with the capability of simultaneous generation of nanostructure gradients, it is necessary to control both material flux and flux gradient of each individual material, as well as the substrate tilt angle with respect to the graded flux. The control and compositional variation can be achieved in an e-beam-based GLAD system, where each material or compound is deposited from its own source, unlike sputtering, where a single multinary target can be used and less variation in composition of the ML is achieved [33]. We have realized such a scheme and this allows us to grow an octonary (8 element), or even higher, ML. The parameter variations of the ML are exemplified by gradients in physico-chemical properties, including optical and wetting properties, as well as electroactivity.

Results and discussion

Combinatorial multinary deposition system

For our method, an electron-beam (e-beam) PVD vacuum system is modified as depicted in Fig. 1a, to incorporate off-axis positioning of the material source relative to the center of the substrate placement, on the *x*-axis (front view), which is crucial for forming an asymmetric vapor flux. A barrier is located between source and substrate, which is combined with the capability for automated GLAD with tilt and rotation of the substrate [10]. To attain a linear gradient, the material source and substrate must be centered on the *y*-axis (side view, Fig. 1a bottom right). The vapor flux gradient is controlled by the position of the barrier that is placed above the material source to shadow part of the outgoing vapor flux towards the substrate. The height of the barrier above the material source, and the distance between the edge of the barrier and the outer diameter of the material vapor flux, *d*, were optimized with the help of Monte Carlo simulations (see SI for details regarding the geometry). The calculations also considered the distance between the material source and the substrate (on the *z*-axis) as well as the tilt angle of the substrate, α. The simulations clearly show that the coverage of the barrier across the vapor source (*d*) is the most important parameter for controlling the vapor flux gradient. The exact numbers depend on the precise chamber geometry, but for a source to sample distance of 580 mm moving the barrier by a few millimeters in either direction already causes extreme changes in the resulting deposition (Fig. S1 SI). In other chambers, with typically less distance, even smaller barrier movements will dramatically affect the gradient. Conversely, the barrier height has a much lower impact on the vapor flux gradient. Here, movements of centimeters (>15 mm) are required to give rise to changes in the vapor flux gradient at a source to sample distance of 580 mm. With optimizations based on simulations, we were able to produce a linear gradient over a substrate length of 50 mm, which is verified experimentally in Fig. 1b, SI Figs. S1 and S2. The glancing angle, α, was set at high angles between 80and 90°, permitting the growth of 3D-nanostructures. After achieving a linear gradient for a single material, the co-deposition with gradients of two materials was implemented. For this purpose, a second barrier was placed on an adjacent source across from the first one, causing the materials to impinge on the substrate with an asymmetric vapor flux (Fig. 1c), to form a binary material system. The position of the second barrier was also optimized with Monte Carlo simulations.

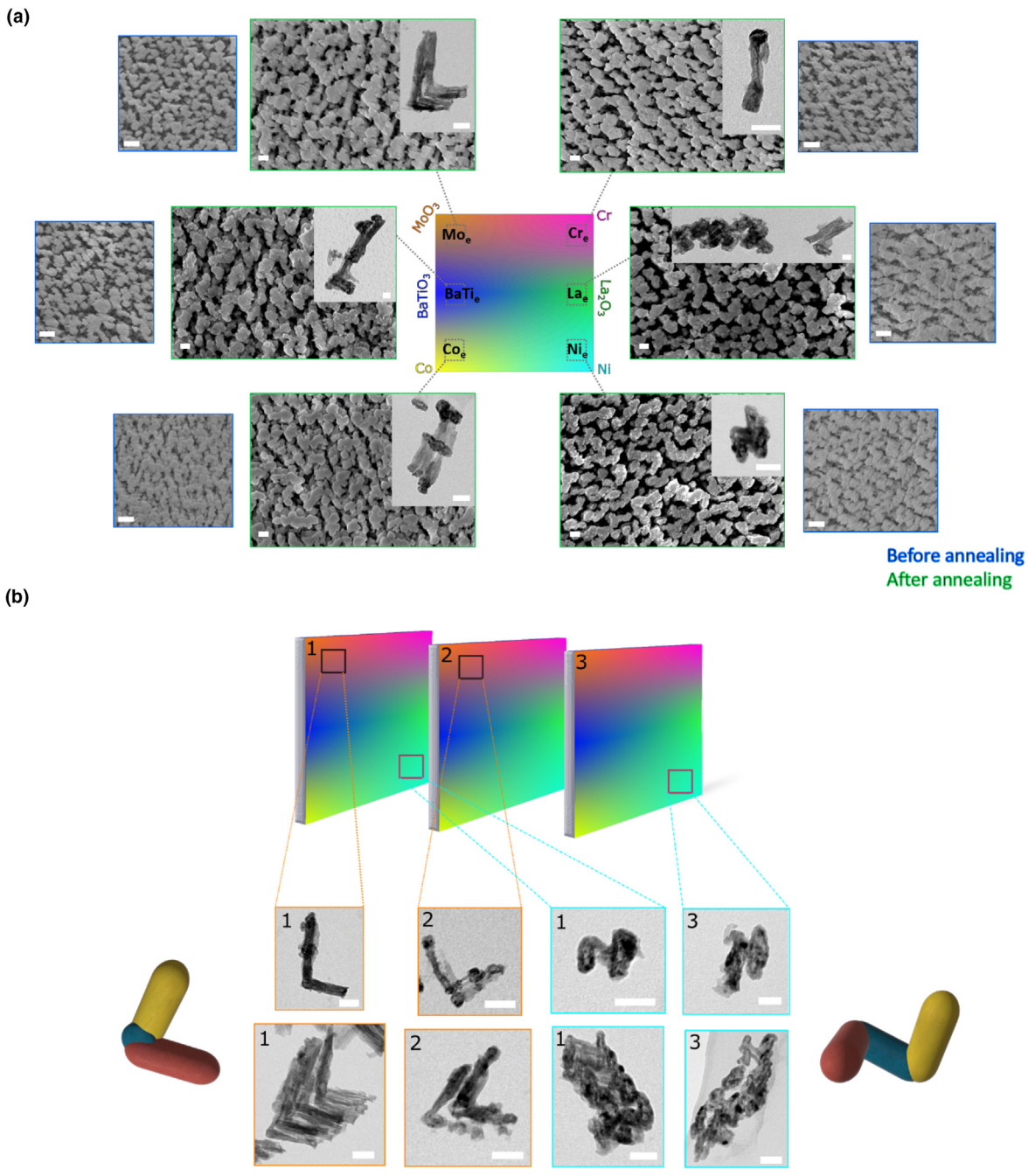

FIGURE 2

Nanostructuring of the octonary materials library. (a) In the center is the schematic of the octonary ML, labeled at the edge with the material that was deposited. Around each edge are the corresponding SEM and TEM micrographs (insets) of the ML after annealing (green frame) and before annealing (blue frame), indicating large changes in the ML surface structuring as well as in the nanoshape for the different edges of the library. The nanoshapes vary from 'zig-zags' to 'match-sticks', have surfaces that look different including 'sphere-like' and triangular. The SEM scale bars are 200 nm- before annealing and 100 nm- after annealing, the TEM scale bar is 50 nm for Co_e, Mo_e, Ni_e, and Cr_e, and 20 nm for $BaTi_e$, and La_e. (b) Schematic of three samples (marked 1–3) produced in the same manner and TEM images from the Mo_e for samples 1 and 2 and Ni_e for samples 1 and 3. The Mo_e all have 'L-shapes' and the Ni_e all have 'zig-zag' nanostructures. TEM scale bar is 50 nm. Left and right are 3D renderings of the Mo_e and Ni_e, respectively, discussed in SI Fig. S5.

To extend the number of material gradients, the substrate is rotated around the ϕ angle (see Fig. 1a). For the octonary ML presented here, a binary deposition step is followed by a rotation of the substrate around the angle ϕ by 120° (while the tilt angle α remains unchanged), and the material sources are exchanged (Fig. 1d). These steps are repeated to increase the number of material elements in the ML. Smaller ϕ rotation angles would enable the number of elements to be further increased. After the last deposition, the ML was annealed to facilitate sub-layer diffusion and to fully oxidize the entire library.

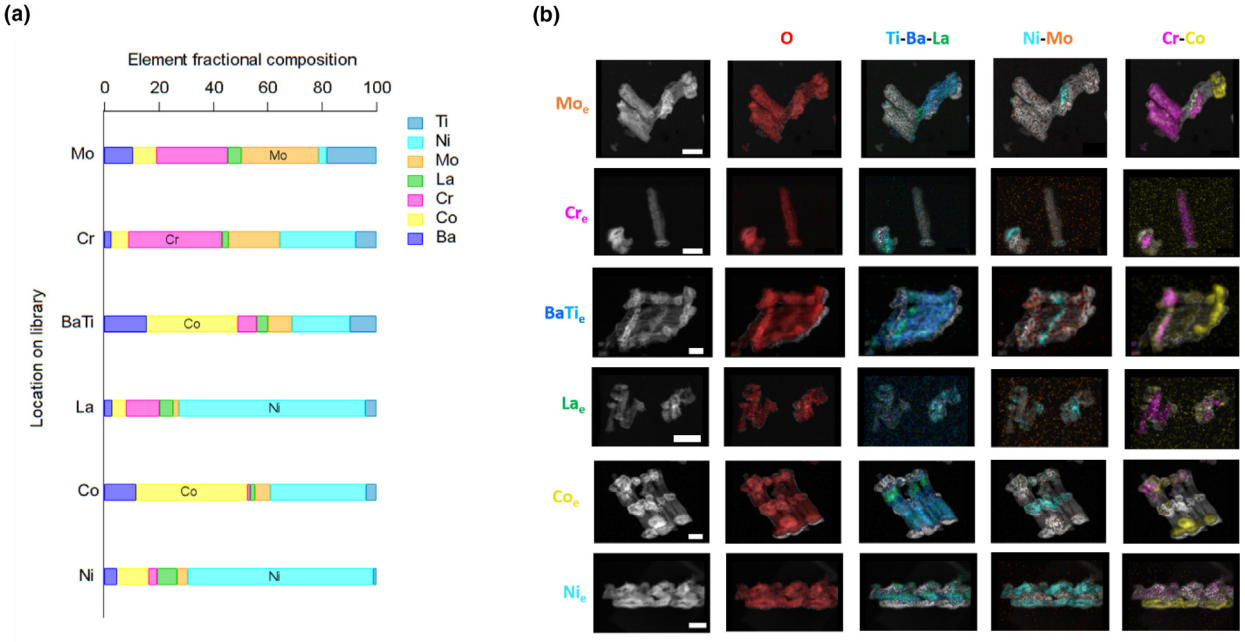

FIGURE 3

Composition of an octonary materials library. (a) Elemental composition of the ML and the different material edges, measured by scanning EDS across the ML under SEM. A gradual change of composition can be seen for each element from its edge and outwards in Fig. S7 SI. (b) Elemental mapping of individual nanoshapes from every edge. Inter-diffusion can be seen for the co-deposited binary layers as well as between the different sub-layers. The slight mismatch between the dark field image and the maps is related to sample drift due to beam damage that occurs during long measurement times. Image scale bars are 50 nm, except for La_e, which is 100 nm.

Nanostructure changes across the library

We demonstrate the method by using six different source materials, $BaTiO_3$, La_2O_3, Ni, MoO_3, Co, and Cr, that are selected for their diversity, their ability to form many compounds, and their widespread use in applications such as catalysis, photovoltaics, and piezoelectrics [34–38]. The co-deposited materials were, a first sub-layer of $BaTiO_3$ (blue-turquoise) and La_2O_3 (green), a second sub-layer of MoO_3 (orange) and Ni (cyan), and a third sub-layer of Co (yellow) and Cr (pink), with 120° rotations between each co-deposited pair, forming an octonary element ML. The maximum gradients of each material are located at the edges of the sample and are marked in the schematic of the sample, Fig. 2a center. To distinguish between the different edges of the sample, the edges (e) are labelled with the source material that shows the highest concentration, for example, $BaTi_e$ denotes the edge where the $BaTiO_3$ gradient is highest (similar to the arrow direction in Fig. 1d). Scanning electron microscopy (SEM) micrographs in Fig. 2a show structural changes on the surface of the different edges. For instance, the Mo_e has elongated structures that are slightly merged, while the Co_e surface has more spherical surface structures. The surface microstructure does not change significantly before and after annealing the sample (SEM images in blue and green frames, respectively), although slight smoothing is seen, probably due to oxygen diffusion into the nanostructures. Transmission electron microscopy (TEM) shows significant variations of the nanoshapes at the different edges. We would like to highlight that the Ni_e nanostructures are zig-zag shaped, as these are later discussed in conjunction with OER. Further details are given in the supplementary information (Figs. S4 and S5 SI). Such a large variety of nanoshapes is seen for the first time on a single substrate in a one-shot deposition. The different nanoshapes that appear at the distinct edges are related to the amount of material flux arriving at an edge, which changes with the deposition rates per material, in conjunction with the shadowing of the substrate and the rotation of the ϕ angle by 120° for every sub-layer deposition. Furthermore, the adatom mobility, which is low since the substrate is maintained at room temperature during the process, also enables the nanoshape formation.

Despite the large variety of materials and shapes, the method can be used to obtain reproducible structures. The reproducibility of this ML growth scheme is highlighted in Fig. 2b. In total, we deposited 10 samples, and several were examined under TEM. The schematic of Fig. 2b shows three different MLs deposited using the same setup and deposition parameters. The TEM micrographs for Mo_e for samples 1 and 2 show the same L-shaped nanostructures and Ni_e shows similar zig-zag structures. Moreover, optical images of two of the samples show the same optical interference patterns (Fig. S6 SI), further emphasizing that the MLs can be reproduced using this setup.

Compositional spread on library and nanostructures

The compositional spread of the whole ML, as well as in individual nanostructures were characterized. Fig. 3a shows the energy dispersive x-ray spectroscopy (EDS) fractional composition for each of the elements in the ML, taken from the different material edges on the substrate. For the Ni_e, Co_e, Mo_e, and Cr_e the highest composition fraction corresponds to the element with the high-

est gradient at that edge. However, for the $BaTi_e$ and the La_e, the highest elemental fraction is from Co and Ni, respectively. These results are expected as the Co_e and Ni_e are adjacent to the $BaTi_e$ and the La_e, respectively. The generally lower $BaTi_e$ and especially La_e compositional fractions can be explained by their higher melting points, which result in lower deposition rates and decomposition of the compounds during the deposition (see SI for more discussion). The compositional features occurred even though the system was calibrated for the individual material depositions prior to the ML deposition. As a general trend, there is an increase in atomic fraction of every element as one approaches the corresponding edge of the substrate. The atomic percentage concentration ranges for the different elements are as follows, Mo 0–28%, Ti 0–36%, Cr 0–35%, Co 2–45%, Ni 2–71%, Ba 0–16%, and La 0–9% (with a 2% error, which is intrinsic to the measurement system we used), and they gradually fall towards the opposite side of the substrate (full compositional maps and more details on the compositional spread are given in Fig. S7 SI).

Element mapping of the individual nanoshapes at every edge (Fig. 3b) clearly shows the location of the respective elements in each nanoshape. It also reveals some (but not full) inter-diffusion between the elements deposited in the binary sub-layers, as well as some inter-diffusion of elements in between the three different sub-layers. Throughout the ML, Mo, Ba, and Ti seem to diffuse between the different layers of the nanostructures and between themselves in a given sub-layer, while Cr, Co, and especially Ni, are more localized, forming clusters within their given sub-layer. In addition, oxygen is homogeneously distributed on all shapes at all edges, indicating that the annealing process completely oxidized the ML. Further discussion and adjacent elements and other elemental mapping combinations can be found in Fig. S8 SI. The elemental maps combined with the TEM structure images (Fig. 2) show that the directionality of the nanostructure growth is governed by the geometry of the shadow growth mechanism. However, the size of the nanostructure is controlled by the properties of the deposited material. These results clearly demonstrate that MLs deposited by GLAD-CMS with compositional gradients are now extended to include gradients in nanostructuring.

Chemical state variations in the materials library

After investigating the broad changes of the nanoshapes and material compositions in the ML, XPS measurements were performed to assess the chemical states of the different elements across the library. XPS analysis was carried out on 9 points across the ML as represented in the schematic of Fig. 4a. Several elements appear with single oxidation states (details in Fig. S9 SI), however the variation in peak intensity indicates that for each material the highest surface concentration is at their corresponding edge. Throughout the ML, both Cr^{+3}, 2p3/2 576.45 ± 0.2 eV (except at point 2, where the shift is 575.6 eV), and Cr^{+6}, 2p3/2 579.6 eV ± 0.3 eV appear [39]. Interestingly, the ratio between the Cr^{+3} to Cr^{+6} changes as one moves away from the Cr_e (Fig. 4b), starting at 2.8:1 for Cr^{+3}:Cr^{+6} (at measurement point 7), to the farthest point from the Ce_e (lowest Cr fraction), which is the Co_e (point 3), where the ratio changes to 0.8:1 and the Cr^{+6} becomes the more dominant species. With a view on the electrochemical properties, discussed later, for the Ni 2p3/2 peak there

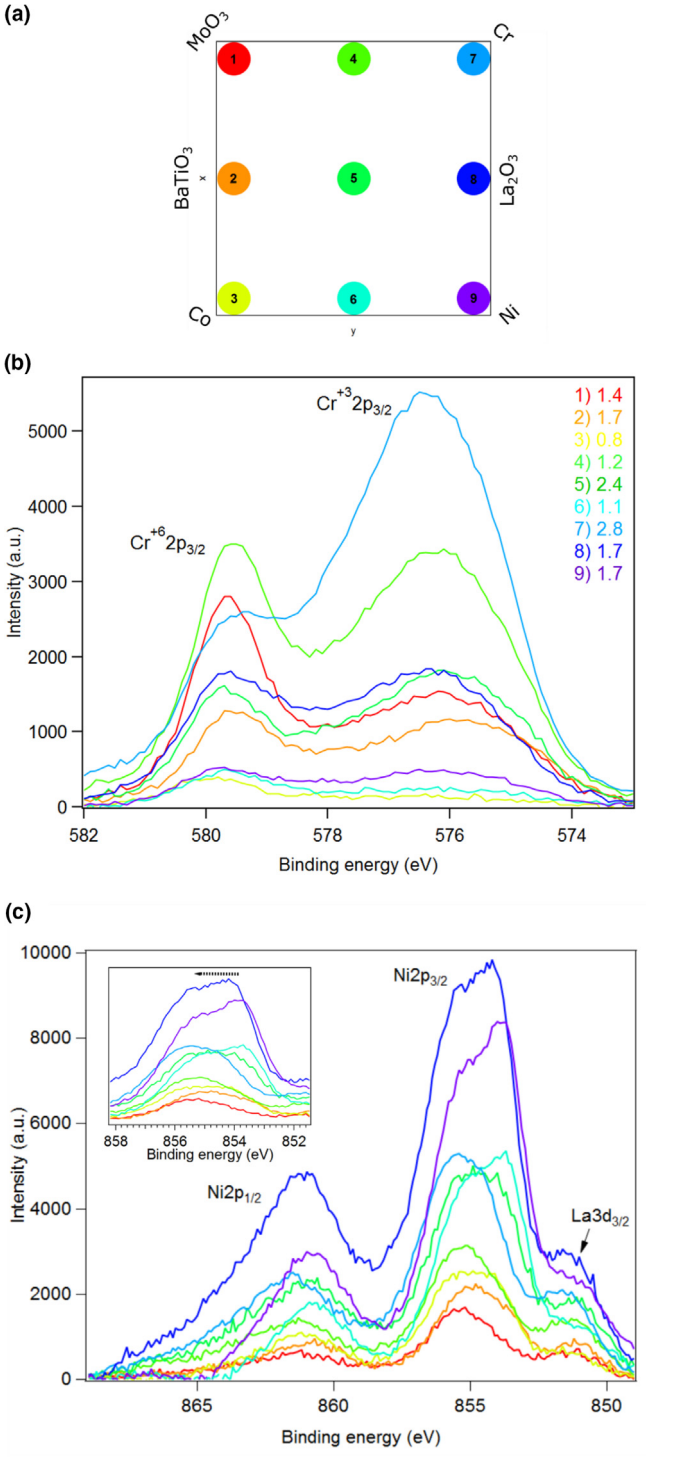

FIGURE 4

XPS analysis of the chemical states in the materials library. (a) Numbered color map of the measurement points taken from the ML for the XPS analysis. (b) Cr 2p3/2 peak, showing the presence of both Cr^{+3} and Cr^{+6} at different ratios in the ML, which change from the Cr_e to the Co_e. The side legend presents the ratios of Cr^{+3}:Cr^{+6} as calculated from the peak areas for measurement points. (c) Ni 2p3/2 peak shifting by 1.6 eV showing how the peak evolves from Ni^{+2} to Ni^{+3} when moving away from the Ni_e. Inset is the enlarged Ni 2p3/2 peak with an arrow indicating the peak shift direction.

is a large shift in peak position from the Ni_e, 853.8 ± 0.02 eV (point 9), to the edge farthest from it (Mo_e), 855.4 ± 0.04 eV (point 1), of 1.6 eV. The shift demonstrates that closer to the

Ni_e, Ni^{+2} is present, while further away Ni^{+3} starts to form and becomes more apparent at the Mo_e [40], although it is not straightforward enough to quantify the ratios between Ni^{+2} and Ni^{+3}. The variation in the chemical state across the ML, related to the large compositional and nanoshape changes in the library, is quite interesting.

Furthermore, we examined the optical and wetting properties of the library, since both are important for various applications including catalysis, and found large variations in optical absorption as well as contact angles (See SI for details, Figs. S11 and S12). The aforementioned properties are essential for many different applications, from (photo)catalysis to magnetism, and as such, it is expected that their gradual change in the ML (arising from composition, nanostructure, oxidation state gradients, etc.) will be an important step in the discovery of new materials.

Electrochemical activity

In order to evaluate the electrochemical activity of the ML and see how the nanostructures and the chemical composition modify the electrochemical response, OER has been selected as a model reaction. We chose the materials in the ML as ones that are active for OER; [41,43] Ni and Co are widely used in their oxide forms, either in pure or in doped oxide form, as catalysts for OER [28,32–36], and La and Ba (as well as $BaTiO_3$) based perovskite oxides are also promising OER electrocatalysts [45–48]. As such, testing an ML composed of gradients of these materials with varying nanostructures as an OER electrocatalyst is the expected following step. First, we tested the OER activity of a porous *vs.* non-porous Pt electrode, in order to understand how nanostructuring (porosity) affects the electroactivity [42]. Both Pt electrodes were deposited using the e-beam GLAD system, where the α angle was kept at 0° to form a thin film flat Pt electrode and at 85° to form a porous Pt nanorod electrode (Fig. S13 SI). The electrochemical measurements were carried out by using a custom-built scanning droplet cell (SDC) system [49–52]. The SDC head, which is composed of the counter and reference electrodes, was moved to predetermined points on the sample in order to measure the electrocatalytic activity of the library. The linear sweep voltammograms (LSV) of the Pt electrodes present the characteristic increase in the current density with onset potentials of 1.82 V and 1.77 V *vs.* a reversible hydrogen electrode (RHE) for flat Pt and Pt nanorods, respectively (Fig. S13a).

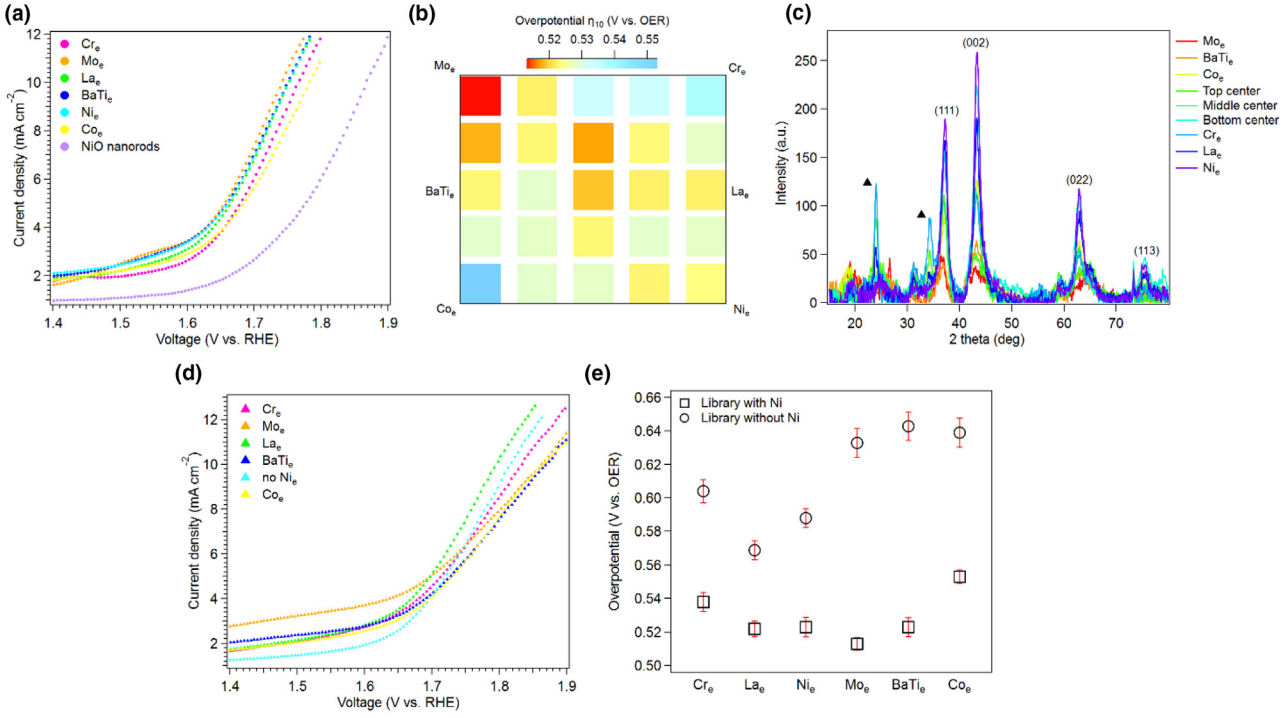

FIGURE 5

Electrocatalytic measurements of the materials library for OER. (a) LSVs of the ML containing Ni and well as a NiO nanorod electrode as reference. The changes in overpotential (η_{10}) across the library are very small, ~40 mV throughout the ML, since the OER activity arises from NiO nanoclusters embedded in the nanostructures of the ML. The overpotential, η_{10}, for the NiO nanorod electrode is ~90 mV higher than the ML, indicating that the NiO nanoclusters in the ML are more active towards OER due to the changes in chemical environment as well as the nanoclustering. (b) Overpotential map of 25 points on the ML containing Ni, showing only a small variation in the η_{10} across the library. (c) Crystal structure of 9 points taken on the ML with Ni by XRD. The main crystal structure is that of NiO, the peak planes are marked. This confirms that NiO nanoclusters form in the nanostructures of the ML, and further supports the fact that they are the main contributors to the OER activity. The two peaks marked with triangles are associated with a slightly distorted phase of $LaNiO_3$, while the other unmarked peaks have not been solved, however they may be associated with Cr based compounds. (d) LSV measurements of the ML without Ni. It is immediately apparent that there are larger variations in the overpotential in this library, due to the chemical changes throughout. This further indicates that the OER activity in the ML containing Ni is governed by the NiO nanoclusters and their surrounding chemical environment. (e) Comparison between the η_{10} overpotentials at the different edges of the MLs with and without Ni. In general, the ML containing Ni has lower overpotentials throughout, owing to the OER activity of NiO nanoclusters. However, the trend in overpotential is similar for both MLs, indicating the effect that the chemical composition at a given edge has on the OER activity for both MLs.

In order to provide a coherent comparison of the overpotentials for OER of both samples, the overpotential at 1 mA cm^{-2} (η_1) was calculated instead of the overpotential at 10 mA cm^{-2} (η_{10}), which is the commonly used method to report overpotentials for OER [53]. A difference in η_1 of 410 mV between flat Pt (η_1 = 0.55 V) and the Pt nanorods (η_1 = 0.14 V) was observed. This change in η_1 is due to the increase in electroactive area, which allows more catalytic sites (with different crystal motifs) to react. A similar improvement in electrocatalytic activity with active surface area has been observed also for multiporous nickel electrodes [54].

Next, we evaluated the electrocatalytic performance for OER at different points of the ML library, by means of LSV and cyclic voltammetry (CV), shown in Fig. 5a and Fig. S14a SI, respectively. As can be seen from a matrix of 25 points measured over the entire ML (Fig. 5b), the η_{10} remains relatively constant, between 0.55 V and 0.51 V. This result is at first sight counterintuitive, as we expected slightly larger changes in overpotential over the full ML, due to the changes in chemical composition. Nevertheless, the obtained η_{10} are quite low and comparable to reported values for NiO nanoparticles (although not within a nanostructured matrix) [55]. When examining the CVs of the different edges (Fig. S14a SI), one can see an oxidation peak appearing between 1.35–1.43 V *vs.* RHE, for all of the edges except the Co_e. This peak has been associated with the formation of Ni^{+3} and Ni^{+5} species, which can indeed occur in the ML, based on the XPS measurements (Fig. 4) [44,56]. As previously seen, the Ni in the library extends throughout the ML with varying composition, but overall has a large compositional fraction (Fig. 3). Furthermore, X-ray diffraction (XRD) measurements of 9 points on the library (Fig. 4a and Fig. 5c) indicate that the dominant crystal structure in the ML is NiO, which implies that this is the main electrocatalytic component in the ML (the two peaks marked with triangles are associated with a distorted phase of $LaNiO_3$, and only appear in 3 points on the library). However, the chemical environment surrounding the NiO is the source of the small variations of η_{10} in the ML, since the NiO is spread within the ML as nanoclusters on the different nanostructures (Fig. 3b). For example, it is located on the ends of the zig–zag structures in the Ni_e, and at the connecting "joints" in the Co_e bone-like structures and the Mo_e L-shape structures.

In order to confirm that the NiO nanoclusters are the source of the OER activity in the original ML, two new samples were prepared; one containing only NiO rod-like nanostructures (composed of smaller NiO nanoparticles, Fig. S15a SI) and a ML library without Ni. For the latter, the setup and deposition parameters were identical to the ML containing the Ni, however no Ni was placed in the chamber for the deposition, and during the fabrication of the second sub-layer only MoO_3 was evaporated. The CV of the NiO nanorods shows the characteristic oxidation peak between 1.0 and 1.2 V *vs.* RHE, confirming the formation of Ni^{+3} and Ni^{+5} species (Fig. S15b SI), whereas the CVs of the different edges of the Ni-free ML do not display such an oxidation peak (Fig. S14b). Furthermore, the NiO nanorods (Fig. 5a, lavender curve) and the ML without Ni (Fig. 5d) show slightly higher overpotentials in comparison with the ones obtained for the ML containing Ni (η_{10} between 0.64 V and 0.57 V, Fig. 5e). Interestingly, the trends from the Cr_e to the Co_e (left to right on the x-axis) are complementary, with an initial decrease in overpotential and then a much higher increase when reaching the Co_e. Such a difference in η_{10} values shows that the electrocatalytic activity for OER is governed both by the nanostructures and the NiO nanoclusters dispersed within, as well as by the chemical composition of the MLs. This important information would not have been obtained without the use of our combinatorial nanostructuring method.

Conclusions

In this work, we present a general and reproducible method for obtaining materials with a continuous variation of composition, nanoshape, and oxidation states, in a one-shot experiment. The technique is based on CMS in conjunction with glancing angle physical vapor deposition and can potentially be adapted to other PVD systems with the proper measurements, calculations, and components. We studied the concept by depositing an octonary ML, with materials used for many applications. The surface nanostructuring and individual nanoshapes of the different edges vary significantly across the library with high reproducibility. The compositional changes are substantial and the different materials inter-diffuse. The oxidation states of some of the materials vary in the ML, where their ratio depends on their location in the library. Optical and wetting properties of the ML show considerable changes and different trends across the library. Investigation of the OER electrocatalytic properties of the ML shows that NiO nanoclusters embedded within the nanostructures are active catalysts for OER and have relatively low overpotentials, which are affected both by nanoclustering and the chemical environment. An ML fabricated without Ni showed OER activity that is dependent on the chemical composition of the ML, indicating that the nanostructure as well as the chemical composition play an important role for electrocatalysis. Prominent changes in the physical properties throughout the library enable the future combinatorial development and optimization of new materials or new combined materials systems, and the method presented here will allow for their rapid direct discovery.

Materials and methods

Materials library fabrication

Libraries were prepared on 50 × 50 mm quartz glass substrates both with, and without, a seeding layer. For electrochemical measurments ITO coated quartz substares were used. The substrates were piranha-cleaned prior to deposition, then dried under N_2 flow. On some substrates, an array of Au nano-dot seeds was deposited by block co-polymer micellar nanolithography (BCML) to facilitate the removal of the nanostructures after growth for TEM imaging. The Au seed patterns were deposited onto the glass substrate from a polystyrene$_{(238)}$-block-poly(2-vinylpyridine)$_{(119)}$ (Polymer Source, Inc.) block co-polymer in o-xylene (Merck) with a concentration of 3.35 mg ml^{-1}, as previously described [27]. The solution (80 μL) was spin-coated onto the substrate at 6000 rpm for 1 min, with an acceleration of 2000 rpm. The Au-polymer substrate was subsequently treated in a plasma system (PVA TePla GIGAbatch microwave plasma system (W10 gas [10% H_2, 90% Ar], 350 W, 0.4 mbar, for 45 min), to reduce the Au salt and remove the polymer, resulting

in an array of ~10 nm Au nanoparticles with distances of 43 ± 9.5 nm between them.

The libraries were prepared in a CMS-GLAD modified system (Thermionics Inc.) with custom-built accessories, with a base pressure of $2{\cdot}10^{-6}$ torr. Six materials ($BaTiO_3$ 99.9%, Alfa Aesar; La_2O_3 99.99%, Arcos Organics; MoO_3 99.95%, Ni 99.995%, Co 99.95%, Cr 99.998%, Kurt J. Lesker Co.) were used as provided and placed in the chamber in six separate crucibles (in two evaporators). The substrate was aligned, based on the position of the barrier, which is situated above the material sources. For every sub-layer a co-deposition of two materials was performed at an α angle of 85°. Thicknesses were monitored using a quartz-crystal microbalance and the ratios between the co-deposited materials was maintained at 1:1 by controlling the deposition rate of each material independent of the other evaporator. After the deposition of a thickness of 30 nm in the binary co-deposition, the substrate was rotated by 120° around the azimuthal angle ϕ and a second co-deposition was started. This was in turn followed by another 120° ϕ angle rotation and co-deposition. The 120° rotation-co-deposition process was repeated 3 times (9 sub-layer depositions in total). The chamber pressure during the deposition was maintained between $8{\cdot}10^{-6}$ and $2{\cdot}10^{-5}$ torr, and the substrate was kept at room temperature. After the deposition, the libraries were rapidly thermally annealed at 500 °C for 10 min (RTP-150-HV annealing furnace, UNITEMP GmBH).

The Flat Pt, Pt nanorod, and NiO nanorod samples were deposited using the same GLAD system and conditions, however the combinatorial shutters were removed from the system. The Flat Pt was deposited at $\alpha = 0°$, the Pt nanorods at $\alpha = 85°$, without any rotation, using Pt 99.99% (Heraeus). The NiO rods were deposited at $\alpha = 87°$ (using Ni as a precursor) and then annealed in a furnace oven at 500 °C for 2 h to form the NiO nanorods (ramp rate 10° per min until set-point was reached and spontaneous cooling).

Nanostructure analysis

The surfaces of the MLs were imaged by a Zeiss Gemini ULTRA 55 SEM and a Zeiss Gemini SEM 500 at an acceleration voltage of 5 kV. For the TEM nanoshape characterization of each individual area, pieces of ~0.5 cm^2 where cut off the specific edges (see Fig. 1) of the library deposited on the seeding layer. TEM samples were prepared by lift-off of the nanostructures in a 1 mM aqueous sodium citrate solution. Each piece of substrate was sonicated for 5 minutes. The resulting nanocolloidal solution was then drop cast (~15 μL) onto a Holey® carbon coated TEM grid (Cu 300 mesh), and left to dry. The sample-loaded TEM grid was washed with deionized water to remove excess salts, and dried. Bright field TEM images were recorded on a Philips CM200 under an accelerating voltage of 200 kV.

Compositional analysis

The ML composition was measured with a high-resolution scanning electron microscope (HRSEM, Magellan 400L, FEI) using an energy dispersive x-ray spectroscopy (EDS) setup in the system. The EDS spectra were obtained with an 80 mm^2 X-max detector (Oxford Instruments). 144 points were measured on the ML at an acceleration voltage of 30 kV, and analyzed using the Aztec software (Oxford Instruments). The elemental maps of the individual nanostructures were obtained by scanning transmission electron microscopy (STEM). The same grids used for the TEM where also used for the STEM measurements. STEM measurements where conducted using a Zeiss SESAM microscope, under an accelerating voltage of 200 kV. High-angle annular dark field STEM (HAADF-STEM) images and STEM energy dispersive X-ray (STEM-eds) elemental maps were recorded with a 20-μm top-hat objective aperture, and at a tilt angle of 20° to maximize the X-ray signal. For the Co and Mo edges, HAADF-STEM imaging, combined with EDS, were carried out at 200 kV with an advanced analytical TEM/STEM (JEOL ARM200F, JEOL Co. Ltd.), equipped with a cold field-emission gun, and a DCOR probe Cs-corrector (CEOS Co. Ltd.). EDX spectra and elemental maps were obtained by acquiring area scans using a 100 mm^2 JEOL Centurio SDD-EDX detector and the Thermo Noran System 7 EDX (Thermo Fisher Scientific Inc.).

Chemical state analysis

XPS measurements, used for analyzing oxidation state and chemical bonding, were carried out on a Theta Probe Angle-Resolved X-ray Photoelectron Spectrometer System (Thermo Fisher Scientific Inc.). The excitation source was non-monochromatic Al K α radiation, operated at 100 W ($h\upsilon = 1486.68$ eV). The base pressure of the system was kept at 3×10^{-10} mbar. The recorded spectra included a survey, acquired at a pass energy of 200 eV, of each measurement point. Subsequently, high-resolution spectra of the different elements were acquired at 50 eV, for every measurement point. The charge referencing was corrected for the binding energies of all the elements for all measurement points, by setting the C–C (or C–H) constituent of the C 1s peak to 284.8 eV [57]. The quantitative surface chemical analysis, performed using the Avantage software, consisted of removing a non-linear Shirley background, from the high-resolution core-level spectra of each of the elements in every measurement point. After which, the analysis and peak fitting was performed by the Powell method, which we found to be robust.

Crystal structure measurements

The ML was measured by XRD using a D8 Discover DaVinci system (Bruker). A parallel beam path was used with a Cu 2 kW tube and a tube energy of 40 kV (40 mA). A detector slit of 9 mm was used for the LynxEye detector (Bruker, 1D mode). Scans were performed in the grazing incidence (GI) in order to detect the nanostructured thin film, this resulted in peak broadening. The scans were taken with a GI Omega of 1–5, the 2theta angles were 15–80°. Analysis was performed using CrystalDiffract software (V. 6.8.1, CrystalMaker Software Ltd.), and peak association was done using the Crystallography Open Database (COD) [58–63], NiO entry COD ID 1010095, $LaNiO_3$ entry COD ID 1000307.

Electrochemical measurements

CV and LSV experiments were conducted using a custom-built scanning droplet cell (SDC) setup. The system consists of the SDC head, which has a spiral Pt counter electrode (cleaned in 1:4, H_2O_2 30%: H_2SO_4 97%, respectively, prior to experiments), an Ag/AgCl (3 M NaCl) reference electrode, and a Teflon cap tip, which touches down to the sample surface and its contact

area is considered as the working electrode area (see Fig. S16 SI for working electrode area measurement details). A micro tube is attached to the SDC from one side and to a pump from the other side. The pump delivers the electrolyte solution into the SDC and also washes electrolyte in between measurements. Furthermore, a force sensor (2 N) is connected to the SDC head and controls the pressure the SDC head applies on the sample when touching down, here we use forces of 150–250 mN for the measurements. All the above-mentioned parts were purchased from Sensolytics GmbH. The SDC is attached to *X–Y–Z* integrated long travel stages (150 mm travel, ThorLabs GmbH), which control the positioning of the SDC over the samples. The system is also connected to an Autolab potentiostat (PGSTAT204, Metrohm) and the measurements were performed with the help of Nova software (2.1, Metrohm). The electrolyte was 0.1 M KOH (pH = 13) in MilliQ water, which was bubbled with Ar for at least half an hour before the experiment, and during the measurement Ar was flowing inside as well. The CVs were recorded at a scan rate of 10 mV s^{-1}, with a step of 5 mV, for 10 cycles, followed immediately by the LSV scan performed under the same conditions. All potentials are corrected with respect to RHE using the equation, $E_{RHE} = E_{Ag/AgCl} + (0.059 * pH) + E°_{Ag/AgCl}$, where $E_{Ag/AgCl}$ is the measured potential *vs*. Ag/AgCl and $E°_{Ag/AgCl}$ is the potential of Ag/AgCl (in 3 M NaCl) *vs*. RHE, taken 0.21 V for our calculations. The overpotentials for OER were calculated by taking the measured potentials *vs*. RHE and subtracting from them the thermodynamic potential of the OER, $E°$ = 1.23 V. The current was normalized to the geometric area of the working electrode, which was found to be 0.0022 cm^2 (See SI Fig. S16).

Data availability

The raw/processed data required to reproduce these findings cannot be shared at this time due to legal or ethical reasons. However, data may be shared upon request from corresponding author.

CRediT authorship contribution statement

Hannah-Noa Barad: Conceptualization, Methodology, Validation, Formal analysis, Investigation, Funding acquisition, Visualization, Writing - original draft, Writing - review & editing, Project administration. **Mariana Alarcón-Correa:** Investigation, Formal analysis, Validation, Writing - review & editing. **Gerardo Salinas:** Investigation, Formal analysis, Writing - review & editing. **Eran Oren:** Methodology, Investigation, Validation, Software, Writing - review & editing. **Florian Peter:** Investigation, Formal analysis, Validation, Writing - review & editing. **Alexander Kuhn:** Supervision, Resources, Funding acquisition, Writing - review & editing. **Peer Fischer:** Conceptualization, Supervision, Resources, Writing - review & editing.

Declaration of Competing Interest

The authors declare that they have no known competing financial interests or personal relationships that could have appeared to influence the work reported in this paper.

Acknowledgments

H.N.B. would like to acknowledge the Minerva Stiftung Fellowship for funding this research. M.A.C would like to acknowledge the Vector Stiftung for their financial support. The authors thank C. Miksch for assistance with BCML. The authors would like to thank A. Itzhak and A. Kama for their support with EDS and optical measurements, as well as P. Schuetzenduebe for conducting the XPS measurements, G. Maier for the XRD measurements, and M. Alomari for performing the RTA. The authors would like to express their gratitude to P. van Aken for access to the Stuttgart Center for Electron Microscopy (StEM) and K. Hahn for the STEM measurements. The authors also thank A. Posada Boada for composing the 3D rendering of the nanostructures and V.M. Kadiri for optical images. The authors appreciate the scientific discussions with A.G. Athanassiadis, H. Kwon, and Z. Ma. The authors also acknowledge partial funding by the European Research Council (ERC) under the European Union's Horizon 2020 research and innovation program (grant agreement no 741251, ERC Advanced grant ELECTRA).

Appendix A. Supplementary data

Supplementary data to this article can be found online at https://doi.org/10.1016/j.mattod.2021.06.001.

References

[1] I. Takeuchi, J. Lauterbach, M.J. Fasolka, Mater. Today 8 (2005) 18–26.
[2] E. Reddington et al., Science 280 (1998) 1735–1737.
[3] W.T. Hong et al., Energy Environ. Sci. 8 (2015) 1404–1427.
[4] S. Rühle et al., J. Phys. Chem. Lett. 3 (2012) 3755–3764.
[5] M. Jansen, Angew. Chem., Int. Ed. 41 (2002) 3746–3766.
[6] T. Kuykendall et al., Nat. Mater. 6 (2007) 951–956.
[7] A. Ludwig, NPJ Comput. Mater. 5 (2019) 70.
[8] R. Potyrailo et al., ACS Comb. Sci. 13 (2011) 579–633.
[9] Z.H. Barber, M.G. Blamire, Mater. Sci. Technol. 24 (2008) 757–771.
[10] S. Guerin, B.E. Hayden, J. Comb. Chem. 8 (2006) 66–73.
[11] S. Siol, et al., Adv. Mater. Interfaces (2016) 1600755 (1–5).
[12] H. Kumigashira et al., J. Electron Spectrosc. 136 (2004) 31–36.
[13] H. Stein et al., Phys. Status Solidi A 212 (2015) 2798–2804.
[14] A. Kafizas, G. Hyett, I.P. Parkin, J. Mater. Chem. 19 (2009) 1399–1408.
[15] C.H. Olk, D. Haddad, J. Alloys Compd. 417 (2006) 235–240.
[16] C.H. Olk, D.B. Haddad, J. Mater. Res. 21 (2006) 1221–1228.
[17] G. Liu, et al., J. Appl. Phys. (2019) 114108 (1–7).
[18] F. Mao et al., Appl. Mater. Interfaces 8 (2016) 30635–30643.
[19] M. Carmo et al., ACS Nano 5 (2011) 2979–2983.
[20] P. Kumar et al., Coord. Chem. Rev. 353 (2017) 113–141.
[21] K. Biswas et al., Nature 489 (2012) 414–418.
[22] C. Burda et al., Chem. Rev. 105 (2005) 1025–1102.
[23] V. Amendola et al., J. Phys. Condens. Matter 29 (2017) 203002.
[24] S. Mubeen et al., Nat. Nanotehnology 8 (2013) 247–251.
[25] M.M. Hawkeye, M.T. Taschuk, M.J. Brett, Glancing Angle Deposition of Thin Films Engineering the Nanoscale, John Wiley & Sons Ltd., West Sussex, 2014.
[26] J.G. Gibbs et al., Nanoscale 6 (2014) 9457–9466.
[27] A.G. Mark et al., Nat. Mater. 12 (2013) 802–807.
[28] Y. Motemani, et al. Nanotechnology 27 (2016) 495604 (1–13).
[29] C. Khare, et al. Nanotechnology 28 (2017) 185604 (1–13).
[30] S. Larson, W. Huang, Y. Zhao, Nanotechnology 27 (2016) 365304 (1–11).
[31] A.I. Mardare et al., Appl. Surf. Sci. 499 (2020) 143943.
[32] H.H. Jeong et al., ACS Nano 13 (2019) 11453–11459.
[33] T.X. Nguyen et al., ACS Comb. Sci. 22 (2020) 858–866.
[34] M. Acosta et al., Appl. Phys. Rev. 4 (2017) 041305.
[35] J. Haber, E. Lalik, Catal. Today 33 (1997) 119–137.
[36] A. Mittasch, W. Frankenburg, Adv. Catal. 2 (1950) 81–104.
[37] Y.-Z. Su et al., Electrochim. Acta 174 (2015) 1216–1224.
[38] B. Kupfer et al., Adv. Energy Mater. (2014) 1401007.
[39] M. Ma, Y. Chen, Y.-M. Cui, Chin. Phys. B 27 (2018) 057702.
[40] H.-N. Barad et al., ACS Comb. Sci. 20 (2018) 366–376.

[41] I. Roger, M.A. Shipman, M.D. Symes, Nat. Rev. Chimstry 1 (2017) 1–13.
[42] W. Jin et al., J. Phys. Chem. B 116 (2012) 7531–7537.
[43] N.-T. Suen et al., Chem Soc 46 (2017) 337–365.
[44] D. Xu et al., Electrochim. Acta 265 (2018) 10–18.
[45] M.P. Browne, C. Domínguez, P.E. Colavita, Curr. Opin. Electrochem. 7 (2018) 208–215.
[46] A. Wattiaux, et al., J. Electrochem. Soc. 134 (n.d.) 1714–1718.
[47] S. Yagi et al., Nat. Commun. (2015) 1–6.
[48] X. Cheng, et al. InSchmidt, (2018).
[49] A.S. Bandarenka et al., Analyst 139 (2014) 1274–1291.
[50] J.M. Gregoire et al., Rev. Sci. Instrum. 84 (2013).
[51] M. Woodhouse, G.S. Herman, B.A. Parkinson, Chem. Mater. 17 (2005) 4318–4324.
[52] M. Woodhouse, B.A. Parkinson, Chem. Soc. Rev. 38 (2009) 197–210.
[53] Y. Gorlin, T.F. Jaramillo, J. Am. Chem. Soc. 132 (2010) 13612–13614.
[54] S. Assavapanumat et al., ChemCatChem 11 (2019) 5951–5960.
[55] J. Masa et al., Angew. Comm. 53 (2014) 8508–8512.
[56] X. Lu, C. Zhao, Nat. Commun. (2015) 1–7.
[57] G. Greczynski, L. Hultman, Prog. Mater. Sci. 107 (2020) 100591.
[58] R.T. Downs, M. Hall-Wallace, Am. Mineral. 88 (2003) 247–250.
[59] S. Gražulis et al., J. Appl. Crystallogr. 42 (2009) 726–729.
[60] S. Gražulis et al., Nucleic Acids Res. 40 (2012) D420–D427.
[61] S. Gražulis et al., J. Appl. Crystallogr. 48 (2015) 85–91.
[62] A. Merkys et al., J. Appl. Crystallogr. 49 (2016) 292–301.
[63] M. Quirós et al., J. Cheminform. 10 (2018) 23.